I&EC research

Industrial & Engineering Chemistry Research

Hydrodynamic Study of Single- and Two-Phase Flow in an Advanced-Flow Reactor

Ke-Jun Wu,[†] Valentina Nappo,[†] and Simon Kuhn*[,†,‡]

[†]Department of Chemical Engineering, University College London, Torrington Place, London WC1E 7JE, U.K.
[‡]Department of Chemical Engineering, KU Leuven, W. de Croylaan 46, 3001 Leuven, Belgium

ABSTRACT: The hydrodynamics of the G1 fluidic module of the Corning Advanced-Flow reactor (AFR) was characterized using particle image velocimetry. Two series of experiments, single-phase flow with liquid flow rates of 10−40 mL/min and two-phase flow with an identical overall flow rate range and gas volume transport fractions ranging from 0.125 to 0.50, were performed. From the instantaneous velocity vector maps, the mean and the root-mean-square velocities were computed, which allowed a systematic investigation of the single- and two-phase flow hydrodynamics and transport processes in the AFR. In single-phase flow, the velocity field is symmetric in the heart-shaped cells, and their particular design results in a stagnation zone that limits momentum exchange in each cell. The addition of the gas phase greatly increases the momentum exchange in the heart-shaped cells, which leads to a more uniform distribution of velocity fluctuations and increased transport processes within the AFR.

INTRODUCTION

In the past two decades, there has been an increased interest in research on microfluidic technology for use in chemical synthesis from laboratory-scale to large-scale production.[1−4] Microfluidic devices, as understood herein, refer to fluidic devices over a scale ranging from microns to a few millimeters, or more specifically in the range of about 10 μm to about 2 mm.[5] Some key microfluidic devices that have been used in large-scale production include the Corning Advanced-Flow reactor (AFR) (solketal *tert*-butyl ether, 12 kg/h),[6] the Forschungszentrum Karlsruhe (FZK) reactor (polymer intermediate, 30 tons/week),[7] Alfa Laval Plate Reactor or Open Plate Reactor (sodium sulfate, ~5 kg/h),[8] the IMM cylindrical falling film microreactor (nitroglycerine, 15 kg/h),[9] and Ehrfeld BTS MIPROWA systems (10−10000 L/h).[10] The aforementioned reactor systems are characterized by various channel geometries, diverse mixing and heat exchange designs, and thus distinctive scale-up strategies. For each reactor, some particular application instances have been reported,[11−13] but research on their hydrodynamic behavior and related transport processes, especially when advancing from single- to two-phase flow, is largely missing, which may become an important factor in restricting the spread and application of these reactors.

From among a few commercially available options, the Corning AFR (G1 fluidic module) was used in this study. A typical AFR module is an assembly of four structured and surface-modified glass plates, forming two heat exchange layers with a reaction layer sandwiched in between (see Figure 1), and the limited opaqueness of the assembly allows the use of particle image velocimetry (PIV) for optical characterization of the flow field. In microfluidic devices, the length scales of the flow passages are very small and their geometries are complicated, and thus conventional, invasive flow diagnostic tools cannot be used for fluid flow characterization.[14,15] One of the most popular noninvasive methods for fluid flow characterization is PIV, which is based on multiple recordings of particle
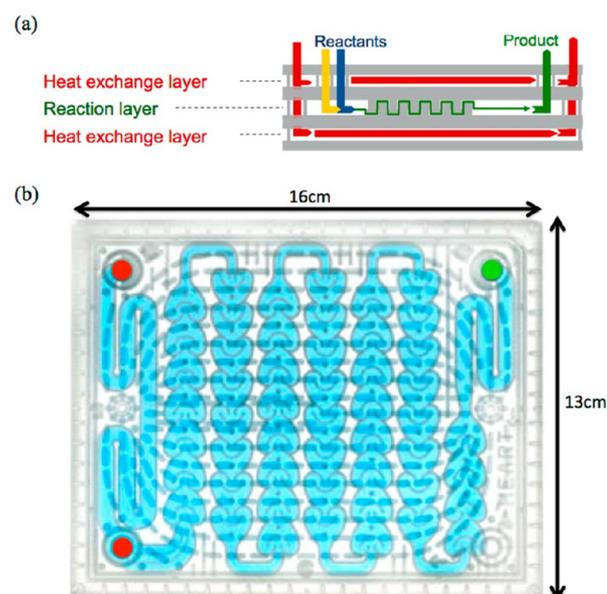
Figure 1. (a) Cross-sectional view of the Corning AFR module showing the two heat exchange layers and the reaction layer. (b) Top view of the Corning AFR module. The two inlets are marked in red and the outlet in green.

images tracing the flow field in the region of interest.[14,16] These small seeding particles are assumed to follow the fluid flow without interference, which means that the particle velocity, which is determined by PIV, is identical to the local fluid velocity. The particles pass a light sheet generated by a laser, and the light scattered from their surfaces is recorded on the
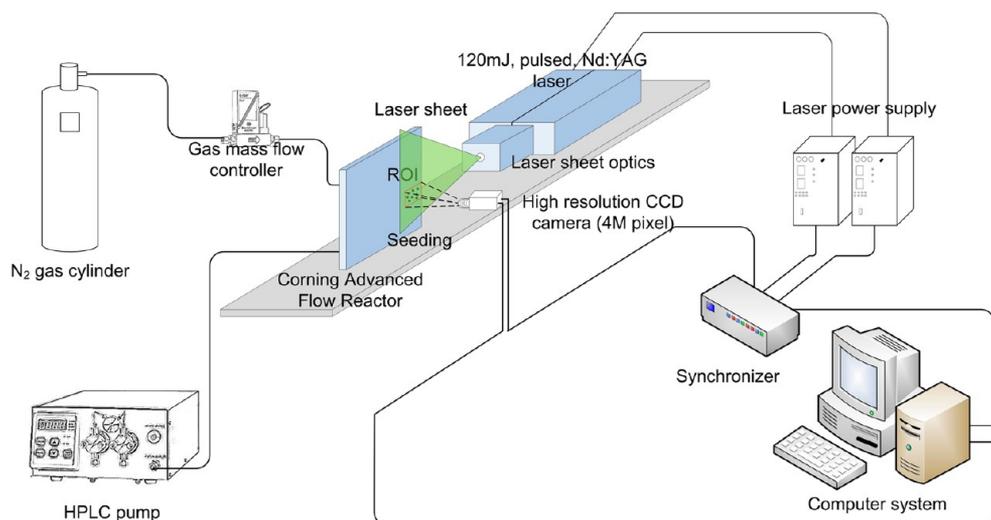
Figure 2. Schematic diagram of the experimental PIV setup.

CCD chip of a digital camera. The light sheet is illuminated twice by two laser pulses, giving a pair of separate images, and the local displacement vectors of the particles can be obtained by a local cross-correlation of two subsequent images. This technique has been successfully applied to single- and two-phase flows in microfluidic geometries to investigate the underlying physics of transport processes.[17,18] The Corning AFR has been previously studied using experimental and numerical means: Zhang et al.[19] evaluated the mixing performance of immiscible liquids in the AFR through extraction efficiency measurements, and Chivilikhin et al.[20] presented a computational fluid dynamics (CFD) analysis of the velocity field, pressure drop, and heat transfer coefficient in the AFR in comparison with experimental results. Nieves-Remacha et al.[21,22] explored drop/bubble sizes and distributions, specific interfacial areas, and mass transfer coefficients of liquid−liquid and gas−liquid two-phase flow in the AFR and found that in comparison with other commonly used two-phase flow contactors the AFR showed enhanced interfacial transport properties. Woitalka et al.[23] compared the liquid−liquid mass transfer coefficients and extraction efficiency of the AFR with those of two microreactors and a Corning Low-Flow reactor. The results showed that the particular design of the AFR enhances the liquid−liquid phase dispersion and thus positively affects the interfacial mass transfer, which allows direct scaling of the mass transfer coefficient $k_L a$ from the microscale. However, the lack of spatially resolved experimental data on the flow field in single-phase and especially multiphase flows in the AFR limits the understanding of local transport processes and their connection to the reactor design, especially taking into account the fact that multiphase CFD approaches are still computationally very expensive.

In this paper, we present for the first time PIV flow field characterization for both single-phase (water) flow and gas−liquid two-phase (nitrogen + water) flow in the AFR. Because of the complex optical setup and corresponding elaborate postprocessing procedure, we additionally validated the experimentally obtained single-phase flow results with CFD simulations. We achieved quantitative agreement between the numerically and experimentally obtained single-phase velocity fields and thus extended this study to PIV in gas−liquid flows to study the variation of mixing and the dispersion character-istics upon the introduction of an inert gas phase, which is considered to be an efficient method to improve liquid mixing performance.[24−26]

■ EXPERIMENTAL SETUP

Corning AFR. The Corning AFR (G1 fluidic module) consists of three layers: the top and bottom ones are the heat transfer layers, and the middle one is the reaction layer. The reaction layer is composed of a series of heart-shaped cells (seven rows and 51 cells in total) having variable cross sections and internal obstacles, namely, a cylindrical post and a U-shaped structure (see Figure 1). Within each heart-shaped cell, the fluid is mixed by splitting and recombining together with the change in velocity direction. The internal volume of the AFR is 8.7 mL, with an experimentally determined channel height of 1.2 mm and a nozzle size of 1.0 mm. The designed flow rates for the reaction layer range from 30 to 200 mL/min, and the operation temperatures and pressures are −60 to 200 °C and 0−18 bar, respectively.

PIV System. The PIV system used in this work was provided by TSI and consists of a pulsed Nd:YAG laser (λ = 532 nm, 120 mJ pulse energy) for illumination, including a light arm for easy manipulation of the laser beam and a range of light-sheet optics. The final thickness of the obtained laser sheet is around 1 mm. A high-resolution (2048 pixels × 2048 pixels) CCD frame-straddling PowerView PIV camera (TSI, model 630059) allows data capture at eight recordings per second, and the entire system is controlled by a synchronizer (TSI, model 610035). TSI's Insight 3G/4G software provided the cross-correlation engine and was used for data acquisition and data analysis.

Although the AFR is made out of glass, common seeding particles for PIV measurements, such as hollow glass spheres or silver-coated particles, proved not to be successful. The specially treated reactor walls and the additional presence of the heat exchange layers result in a distinct level of opaqueness of the entire AFR module that blocks the scattered light signal from the seeding particles in the fluid and additionally introduces noise from the wall surfaces (laser light sheet reflections). To avoid these problems, the liquid phase was seeded with fluorescent polystyrene beads with a diameter of 3 μm (TSI, 10070-2). The excitation and emission wavelengths

of these fluorescent particles are 542 and 612 nm, respectively. Equipping the CCD camera with a high-pass filter (cutoff below 545 nm) removed the laser light reflections from the glass surfaces, allowing the light emitted by the fluorescent particles to be isolated. A vector resolution of 241 μm × 241 μm was obtained (24 pixel × 24 pixel PIV interrogation window with 50% overlap) and the field of view covered an area of 41.12 mm × 41.12 mm.

Experiments and Data Processing. A schematic of the experimental setup is shown in Figure 2. Pure water and N_2/H_2O were chosen as working fluids to carry out single- and two-phase flow PIV measurements. Water was pumped at a constant flow rate using an HPLC pump (Scientific Systems, Prep 100). Nitrogen was supplied from a gas cylinder, and the gas flow rate was controlled by a precalibrated mass flow controller (Bronkhorst, EL-FLOW model F-200CV and F-201CV). The pressure drop over the AFR plate was recorded using a digital differential pressure sensor (Comark C9555).

Figure 3 shows an example image acquired by the PIV camera. Despite the use of fluorescent tracer particles, it was
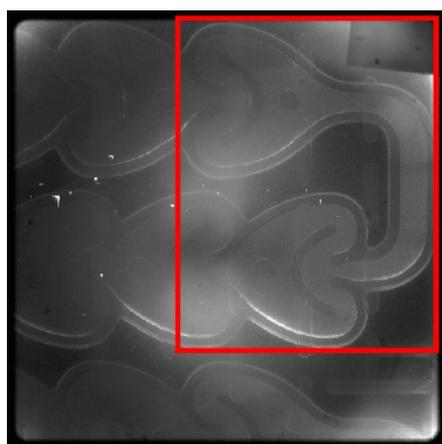
Figure 3. Example image acquired by the PIV camera (frame A) indicating the region of interest (ROI), shown by the red rectangle, which was located at the last heart cell of row 4 and the first heart cell of row 5.

still challenging to obtain sufficient light scattering for the entire reactor plate because of reflection of the laser light sheet from the internal structures of the AFR and the accompanying reduction in incident light intensity. Therefore, the region of interest (ROI), indicated by the red rectangles in Figures 2 and 3, was restricted to the last heart cell of row 4 and the first heart cell of row 5, in which the incident light intensity of the laser

was sufficient to capture processable image pairs, allowing the fully developed flow in the AFR to be studied.

Two series of experiments were performed: the first series of experiments consisted of PIV measurements for single-phase flow at seven liquid flow rates, and the second series of experiments consisted of PIV measurements for two-phase flow with seven overall flow rates and four gas volume transport fractions for each overall flow rate. As the overall channel width of the AFR changes with the position, it is difficult to define a single Reynolds number for the entire reactor. Thus, in this paper we base the Reynolds number on the inlet of the heart cell (channel height h = 1.2 mm, channel width w = 1.0 mm).[22] For all of the experimental conditions, the resulting reference Reynolds number ranges from 150 to 605.

In total, 400 image pairs were recorded for each run, and for single-phase flow we followed the standard postprocessing procedure using TSI's Insight software (spatial calibration, cross-correlation, filtering of erroneous vectors). Although the reference Reynolds number indicates laminar flow, we found temporal velocity fluctuations in the single-phase flow results, indicating the onset of turbulence induced by the specific design of the AFR. Therefore, we decided to use a statistical treatment of the resulting velocity fields by applying Reynolds averaging and decomposing the velocity U into a mean ($\overline{U}$) and a fluctuating part (U'). This procedure allows quantification of the root-mean-square (RMS) velocity fluctuation u_{rms}, which is correlated to momentum transport:

$$u_{\mathrm{rms}} = \sqrt{\frac{\sum_{i=1}^{n}(U - \overline{U})^2}{n}} \quad (1)$$

where n is the number of valid data generated from the 400 image pairs.

In the case of two-phase flow, an additional masking step was added after the above-mentioned processing to remove the bubbles in each image pair, as they do not contain seeding particles and their contribution to the velocity field and the statistical analysis needs to be excluded.[27,28] The image mask was generated using the ImageJ software package,[29] and the main procedures are shown in Figure 4: the raw image (frame A) was used as the source, and in the first step the contrast of the raw image was enhanced using the "Equalize histogram" function. In the second step, Gaussian blur was applied to reduce the image noise, and finally an image mask (black-and-white image) was generated by binarization with adoption of local thresholding. In the ROI, the bubbles were set to be black so that the vectors in the area occupied by bubbles would be excluded from further analysis, and this image mask was applied

Raw image   Image after contrast enhancing   Image after adaptive binarization
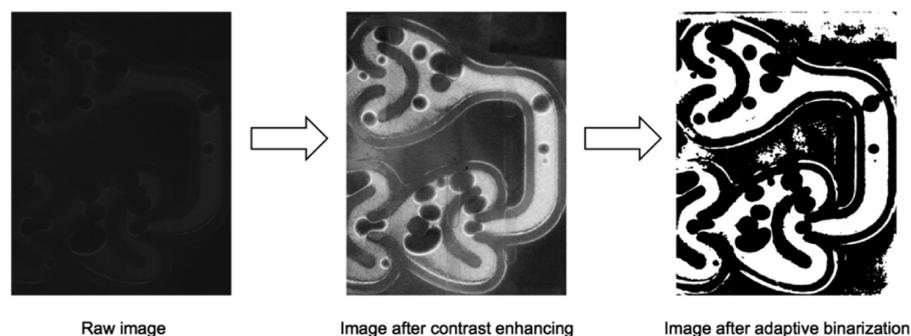
Figure 4. Schematic of the procedure for generation of the image mask.
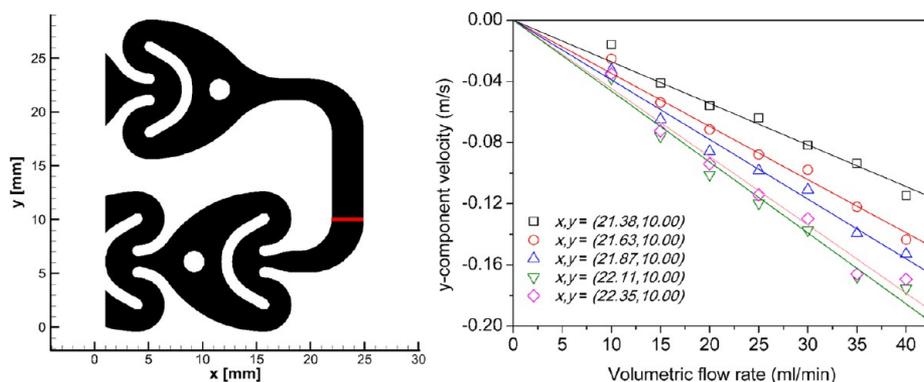
Figure 5. (a) Location in the ROI where the velocities were measured. (b) Relationship between the volumetric flow rates and the local velocities.

to the instantaneous velocity vector maps to remove all velocity information in the bubbles using MATLAB.

RESULTS AND DISCUSSION

In this work, both single- and two-phase flow PIV measurements were carried out. For single-phase flow, seven flow rates (10 to 40 mL/min with intervals of 5 mL/min) were used to investigate the effect of the flow rate on the resulting velocity field. In order to study the variation of mixing and the dispersion characteristics when advancing to two-phase flow, the overall flow rates were kept identical to those for single-phase flow, and four gas volume transport fractions ($\beta = \dot{V}_G/(\dot{V}_G + \dot{V}_L) = 0.125, 0.25, 0.375,$ and 0.50) were used for each overall flow rate. For each flow rate, an ensemble of 400 instantaneous velocity fields was obtained with PIV and subsequently statistically analyzed.

Validation of Single-Phase PIV Measurements. Because of the optical challenges in obtaining PIV data in the AFR module, the reliability of the results was first tested by comparing the velocities in the ROI for different volume flow rates. Five positions in the rectangular channel of the ROI ($y = 10.00$ mm, $x = 21.38-22.35$ mm with intervals of 0.24 mm; Figure 5a) were chosen as examples because the contribution of the x component of the velocity can be neglected at these positions (Figure 5b). Theoretically, the velocity magnitude in each position should increase linearly as the volumetric flow rate increases. It can be seen from Figure 5 that the experimental results are in agreement with theory, as the R^2 values for the linear fits were greater than 0.98 for all of the curves with an intercept equal to 0.

Furthermore, we compared the single-phase flow results with the results of CFD simulations. The computational domain represented the entire reaction layer (see Figure 6), and the computational grid consisted of 1 383 672 prism cells. The hydrodynamic simulations were carried out in OpenFOAM;[30] the built-in solver *simpleFoam* was used, and the simulations were run under steady-state conditions, ensuring convergence of the solutions.

Figure 7 depicts the comparison between experimental and simulation results for a flow rate of 30 mL/min. Since the thickness of the laser sheet was 1 mm (channel height $h = 1.2$ mm) and the PIV technique correlates all of the seeding particles in the illuminated volume, we also present the CFD results volume-averaged along the z-coordinate (from $z = 0.1$ mm to $z = 1.1$ mm) for comparison. Figure 7a,c depicts the mean experimental velocities in the x and y directions ($\overline{u}$ and $\overline{v}$, respectively), whereas Figure 7b,d shows the mean simulation
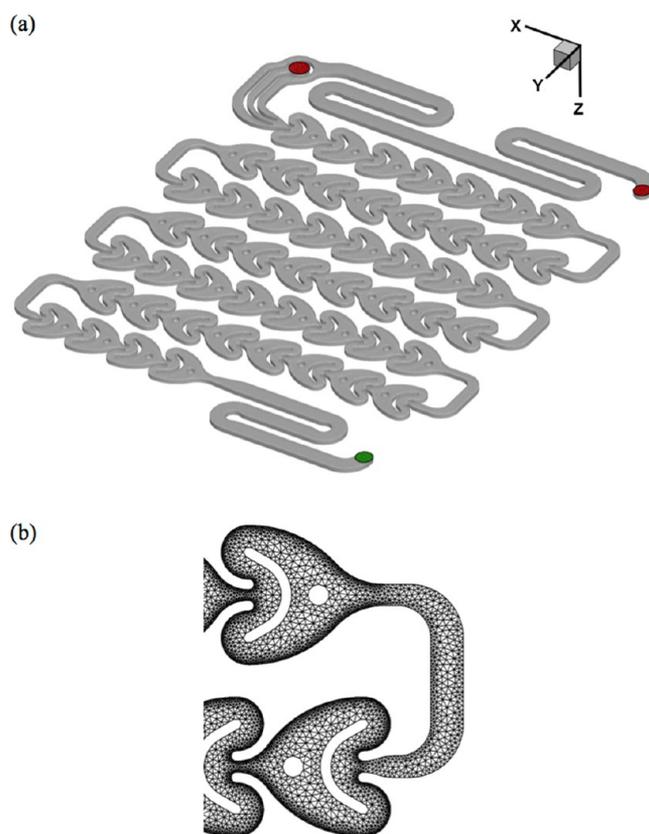
Figure 6. (a) Representation of the computational domain of the AFR used for CFD simulations. The inlets are marked in red and the outlet in green. (b) Computational grid for the ROI of the PIV measurements (last heart cell of row 4 and the first heart cell of row 5).

velocities in the x and y directions, respectively. It can be seen that the PIV experimental results match well with the simulation results not only in the velocity magnitude distribution within the AFR structure but also quantitatively for local velocity values. It has to be noted for the PIV results that because of the presence of the flow distribution structures in the heat exchange layers (see Figure 1b), signals from seeding particles could not be recorded by the CCD camera in some areas, such as the inlet and outlet of the first heart-shaped cell, leading to a discontinuous velocity field in these areas. However, the agreement between the PIV and CFD simulations proved the validity of the applied experimental procedure.
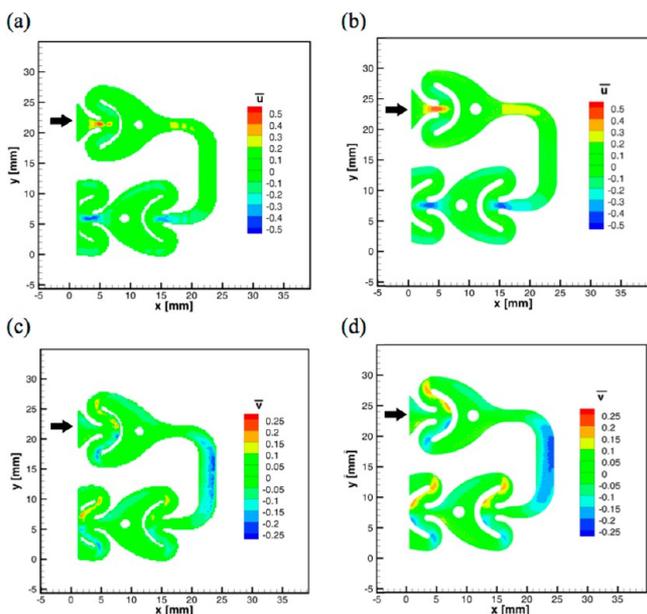
Figure 7. Comparison between PIV (left column) and CFD (right column) results for single-phase flow at a flow rate of 30 mL/min: (a) $\overline{u}$ from PIV; (b) $\overline{u}$ from CFD; (c) $\overline{v}$ from PIV; (d) $\overline{v}$ from CFD.

In the ROI, the fluid travels from left to right and top to bottom. The fluid enters the heart-shaped cell through the narrow inlet, which leads to an increased velocity component in the x direction, as shown in Figure 7a,b. A similar phenomenon can also be observed in the inlet and outlet of each heart-shaped cell. Upon entering the heart cell, the fluid impacts the U-shaped structure, which splits the flow into two streams, one going upward and the other one going downward, that travel with similar velocity magnitudes, as shown in Figure 7b,d. After the U-shaped obstacle, the fluid travels along the reactor walls, leading to a larger velocity near the walls compared with that in the area between the U-shaped structure and the post. After passing the post, the two streams merge again. From Figure 7 it is evident that the velocity field is almost symmetric in the heart-shaped cell and that the influence of gravity on the velocity distribution is insignificant for single-phase flow.[31] Upon exiting the heart-shaped cell, the fluid enters a larger channel, where because of its inertial momentum the fluid near the right wall initially travels faster than the fluid near the left wall. When the fluid enters the next heart-shaped cell, the symmetric velocity distribution is restored. This particular AFR design impacts the mixing and transport processes in single-phase flow, as the presence of the U-shaped structure and the post lead to flow recirculation and stagnation, which broaden the residence time distribution and lead to increased temperature zones (hot spots) in the case of wall heat transfer applications.

PIV Results for Single-Phase Flow. The mean velocity contours for single-phase flow for flow rates of 10, 25, and 40 mL/min are plotted in Figure 8. It should be noted that the contours are plotted on different scales to show detailed features. From Figure 8 it can be seen that the velocity distributions are similar for different flow rates, with the overall velocity magnitude being the only difference. Obviously, the local velocities in both the x and y directions increase with increasing flow rate.

Comparison of Single- and Two-Phase Flow Results for an Overall Flow Rate of 30 mL/min. The two-phase
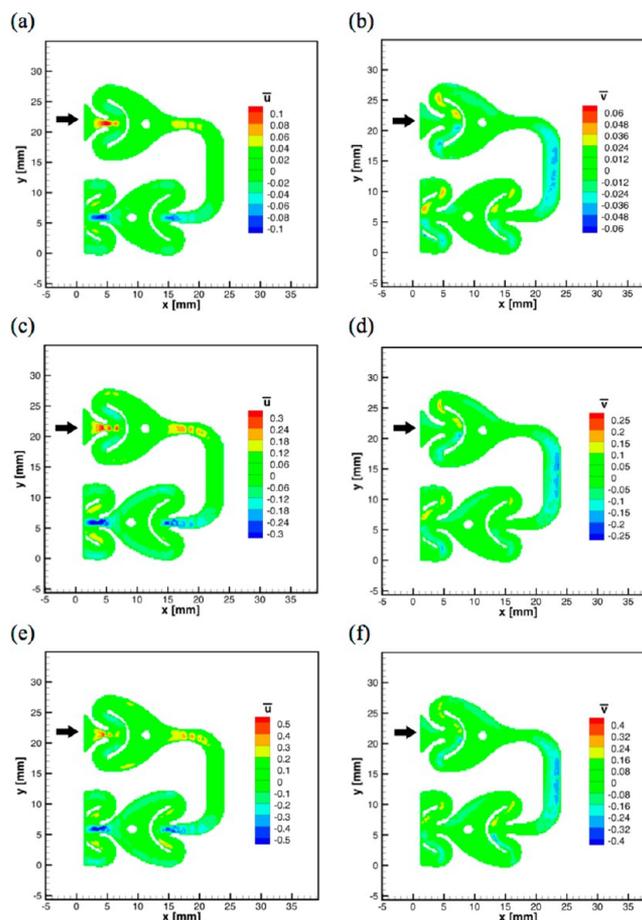
Figure 8. Mean velocity contours for single-phase flow: (a) $\overline{u}$ for 10 mL/min; (b), $\overline{v}$ for 10 mL/min; (c), $\overline{u}$ for 25 mL/min; (d), $\overline{v}$ for 25 mL/min; (e), $\overline{u}$ for 40 mL/min; (f), $\overline{v}$ for 40 mL/min.

flow system with an overall flow rate of 30 mL/min was selected for comparison with the single-phase velocity field results. For each gas volume transport fraction β, one typical image was selected, and these images are depicted in Figure 9. The number-averaged bubble size and the bubble size distribution depend only on the gas and liquid flow rates,[21,32] and increasing the gas flow rate or decreasing the liquid flow rate increases the number-average bubble size and also broadens the bubble size distribution. In this study, as the overall flow rate was constant, the gas volume transport fraction was the only variable. Details about the bubbles for different gas volume transport fractions are listed in Table 1. Although the results in Table 1 are based on only two heart-shaped cells, they also follow the relationship outlined above: when the gas volume transport fraction decreases by 75%, the bubble size and the bubble number in the region of interest decrease by about 25% and 45%, respectively.

To observe the difference between single- and two-phase flow, contour and vector plots are presented in Figures 10 and 11 to show the differences in the magnitude and direction of the velocity. From Figure 10 it can be observed that there are distinct changes in the velocity field when advancing from single- to two-phase flow: (1) The introduction of the dispersed gas phase leads to a decrease in velocity magnitude in some regions of the AFR, especially at the inlet and outlet. This is the case because the fluid resistance in the narrowed channel is enlarged significantly, which slows down the bubble.
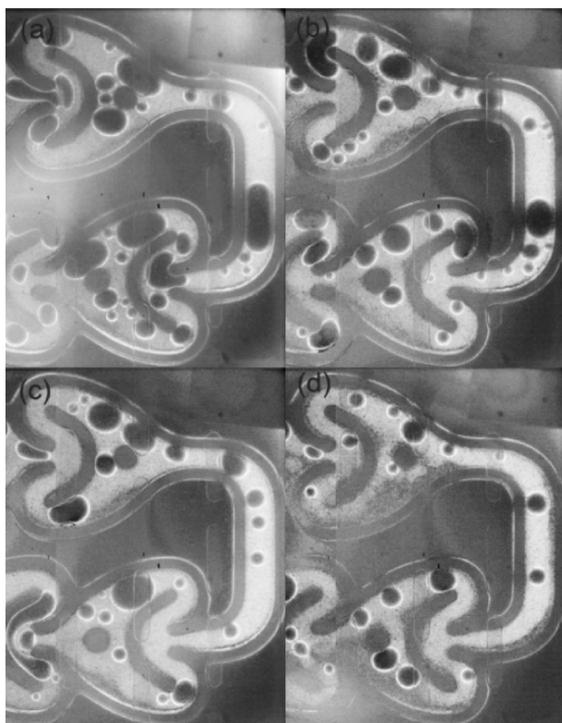
Figure 9. Bubbles in the region of interest with decreasing gas transport fraction: (a) β = 0.50; (b) β = 0.375; (c) β = 0.25; (d) β = 0.125.

Table 1. Bubble Statistics for Four Different Gas Volume Transport Fractions at an Overall Flow Rate of 30 mL/min

β	no. of bubbles	number-averaged bubble size (mm)	standard deviation (mm)
0.50	34	1.857	0.903
0.375	33	1.660	0.730
0.25	26	1.636	0.836
0.125	19	1.394	0.455

(2) Because of gravity, the bubbles preferentially travel along the upper-half of the AFR, and thus, the velocity distributions are no longer symmetric. (3) Increasing the gas volume transport fraction has no significant effect on the velocity magnitude but has an effect on the velocity direction.

Figure 11 depicts a vector plot of the velocity field in which the green arrows represent single-phase flow and the red arrows two-phase flow (β = 0.25). It can be seen that in single-phase flow the fluid travels mainly along the reactor wall, creating a large stagnant flow region between the U-shaped structure and the post. In contrast, for two-phase flow the presence of the dispersed gas bubbles forces the liquid phase in the upper half of the heart-shaped cell to flow downward and that in the lower half to flow upward. Consequently, the local velocities in the region between the two obstacles are increased, thus drastically reducing the stagnant fluid zone.

So far we have restricted ourselves to a discussion of the mean velocity field and the associated changes when advancing from single- to two-phase flow. Earlier studies using the Corning AFR in gas–liquid and liquid–liquid flow proved that this particular design allows direct scaling of the interfacial mass transfer coefficient k_La from the microscale.[21−23] This was attributed to the fact that the AFR design increases the utilization of the dispersed-phase interfacial area. In microfluidic
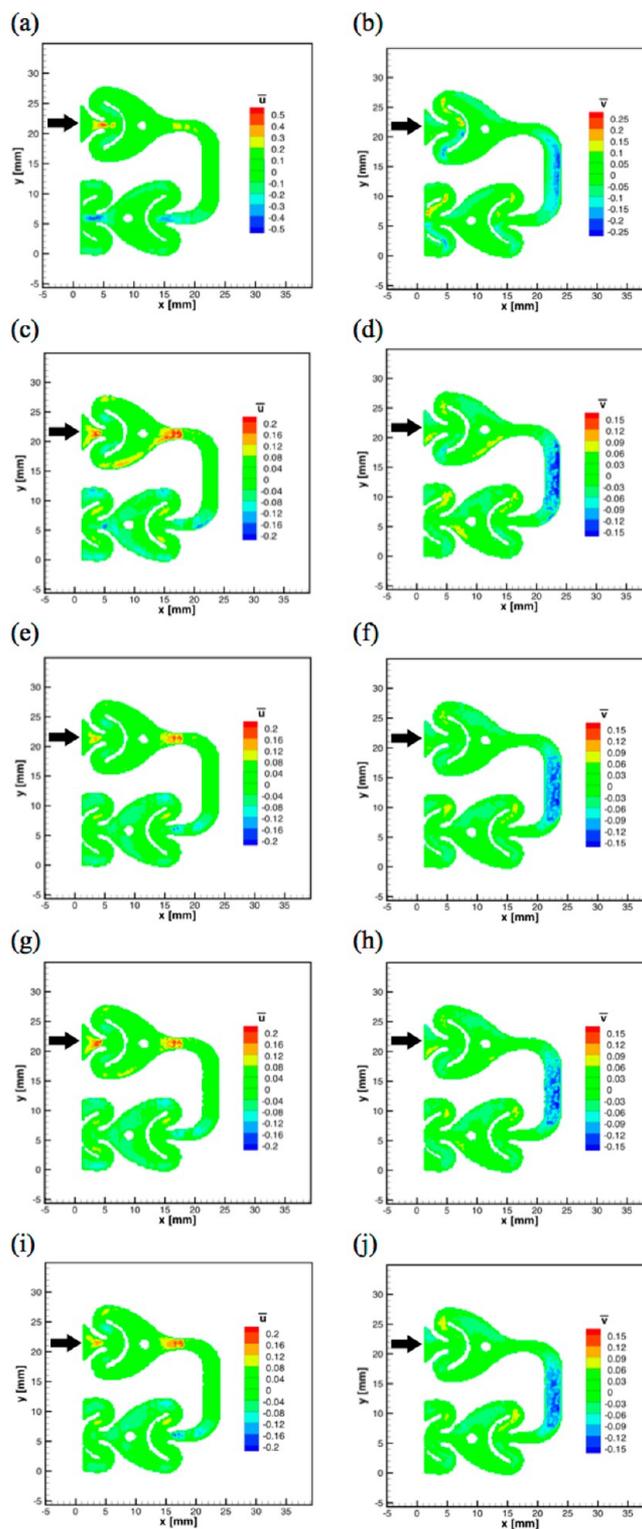
Figure 10. Mean velocities for single- and two-phase flow at an overall flow rate of 30 mL/min: (a) $\overline{u}$ for single-phase flow; (b) $\overline{v}$ for single-phase flow; (c) $\overline{u}$ for β = 0.125; (d) $\overline{v}$ for β = 0.125; (e) $\overline{u}$ for β = 0.25; (f) $\overline{v}$ for β = 0.25; (g) $\overline{u}$ for β = 0.375; (h) $\overline{v}$ for β = 0.375; (i) $\overline{u}$ for β = 0.50; (j) $\overline{v}$ for β = 0.50.

devices, which predominantly feature Taylor flow, mass transfer is mainly restricted to the bubble caps, and the thin liquid film surrounding the bubble makes a limited contribution.[17] In the AFR, because of the constant breakup and merging of the bubbles, the interfacial area is constantly renewed, thus leading
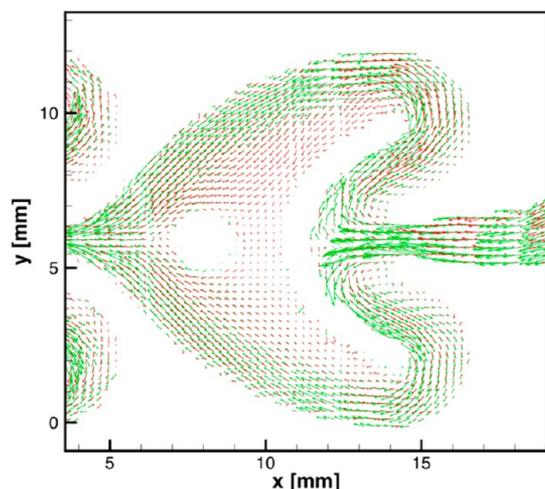
Figure 11. Velocity vector fields of single-phase flow (green vectors) and two-phase flow (β = 0.25) (red vectors) in the first heart-shaped cell of row 5.

Figure 12. Plots of the ratio of the RMS velocity fluctuation magnitudes (two-phase flow/single-phase flow) for an overall flow rate of 30 mL/min: (a) β = 0.125; (b) β = 0.25; (c) β = 0.375; (d) β = 0.50. Dark regions indicate ratios larger than 1, and light regions indicate ratios smaller than 1.

to increased interfacial mass transfer counteracting the increased diffusion paths in the larger geometry. Advancing from these studies and employing the PIV technique, we are able to address mixing in the continuous bulk liquid phase to elucidate the effect of two-phase flow on momentum exchange. This can be quantified by addressing the fluctuating velocity components and computing the RMS velocity, which from a physical point of view is related to the intensity of turbulence and momentum exchange. Besides the momentum exchange caused by the fluid viscosity, there is additional mixing of fluid elements caused by turbulence dispersion due to the instantaneous velocity fluctuations. Larger local u_{rms} indicates a higher turbulence level and thus larger momentum exchange. In short, the larger the local u_{rms}, the better are the mixing and dispersion performance at this position.[33]

To highlight the impact of two-phase flow on the momentum exchange, we computed the magnitude of the RMS velocity fluctuation vector,

$$U_{rms} = \sqrt{u_{rms,x}^2 + u_{rms,y}^2} \tag{2}$$

and the ratios of the RMS velocity fluctuation magnitudes for two-phase flow and single-phase flow are plotted in Figure 12. Dark regions represent values of the ratio greater than 1, i.e., increased mixing in the case of two-phase flow compared with the single-phase case. Conversely, light regions indicate reduced mixing in the case of two-phase flow. We notice that introducing the gas phase increases the fluctuations in most areas of the AFR because of the irregular trajectories and uneven sizes of the bubbles. Only the regions where the mean velocities are large in single-phase flow do we observe a decrease in the level of fluctuations, which is explained by the damping of the velocity jet in the heart inlet section due to the presence of the dispersed gas bubbles (see Figures 10 and 11).

To further aid the quantitative understanding, the average RMS velocity fluctuation magnitude and its standard deviation were calculated, and the values are listed in Table 2. Introducing a gas phase into the AFR does not increase the average RMS velocity fluctuation magnitude but instead reduces its standard deviation. Although the average RMS velocity is roughly 25% larger for the single-phase flow system, the standard deviation is more than 350% larger compared with
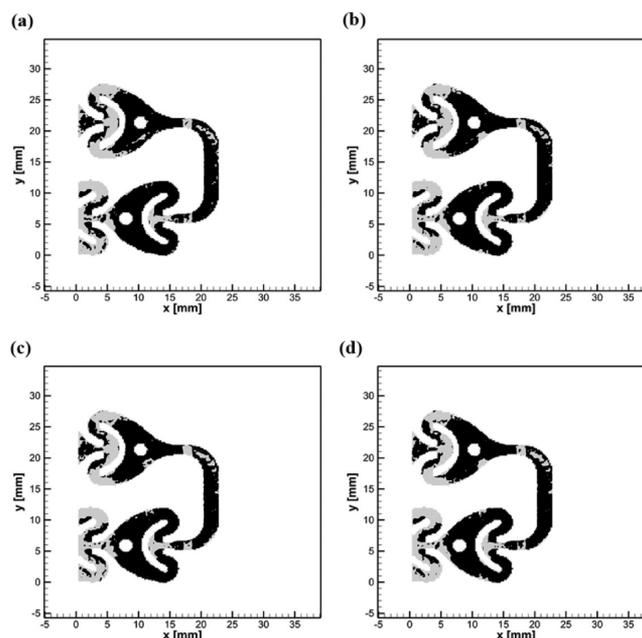
Table 2. Average RMS Velocity Fluctuation Magnitudes and Standard Deviations in the ROI for Single- and Two-Phase Flow with an Overall Flow Rate of 30 mL/min

conditions	average RMS velocity fluctuation magnitude (m/s)	standard deviation (m/s)
single-phase flow	0.0693	0.0871
two-phase flow, β = 0.125	0.0538	0.0187
two-phase flow, β = 0.25	0.0522	0.0154
two-phase flow, β = 0.375	0.0523	0.0164
two-phase flow, β = 0.50	0.0524	0.0159

the two-phase flow system. This means that for single-phase flow, increased momentum exchange and mixing is restricted to certain regions in the AFR, whereas for two-phase flow the intensity of fluctuations is similar within the entire AFR, which consequently leads to good mixing performance in the whole reactor. Increasing the gas volume transport fraction from β = 0.125 to β = 0.50 has no significant effect on the RMS velocity fluctuation magnitude.

Comparison of Single- and Two-Phase Flow for a Gas Volume Transport Fraction of β = 0.25. Next we address the effect of increasing flow rate on the two-phase flow hydrodynamics for a fixed gas volume transport fraction of β = 0.25. One typical image was selected from 400 image pairs for each flow rate to illustrate the bubble distribution, and these images are shown in Figure 13. It can be observed that the overall number of bubbles in the heart-shaped cells increases and their size decreases with increasing flow rate; details about the bubble statistics are listed in Table 3. Together with the data listed in Table 1, these data show that the bubble size increases almost linearly with decreasing flow rate (at fixed β) and increasing β (at fixed flow rate), as illustrated in Figure 14.

To investigate the effect on momentum exchange, the ratios of the RMS velocity fluctuation magnitudes for two-phase and
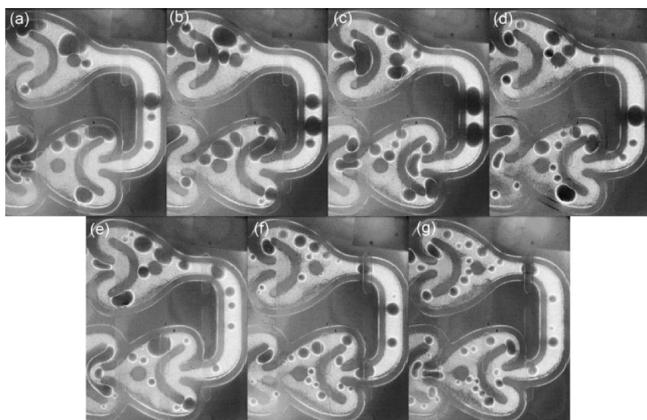
Figure 13. Bubble distributions in the region of interest for a gas volume transport fraction of β = 0.25 at different overall flow rates: (a) 10 mL/min; (b) 15 mL/min; (c) 20 mL/min; (d) 25 mL/min; (e) 30 mL/min; (f) 35 mL/min; (g) 40 mL/min.
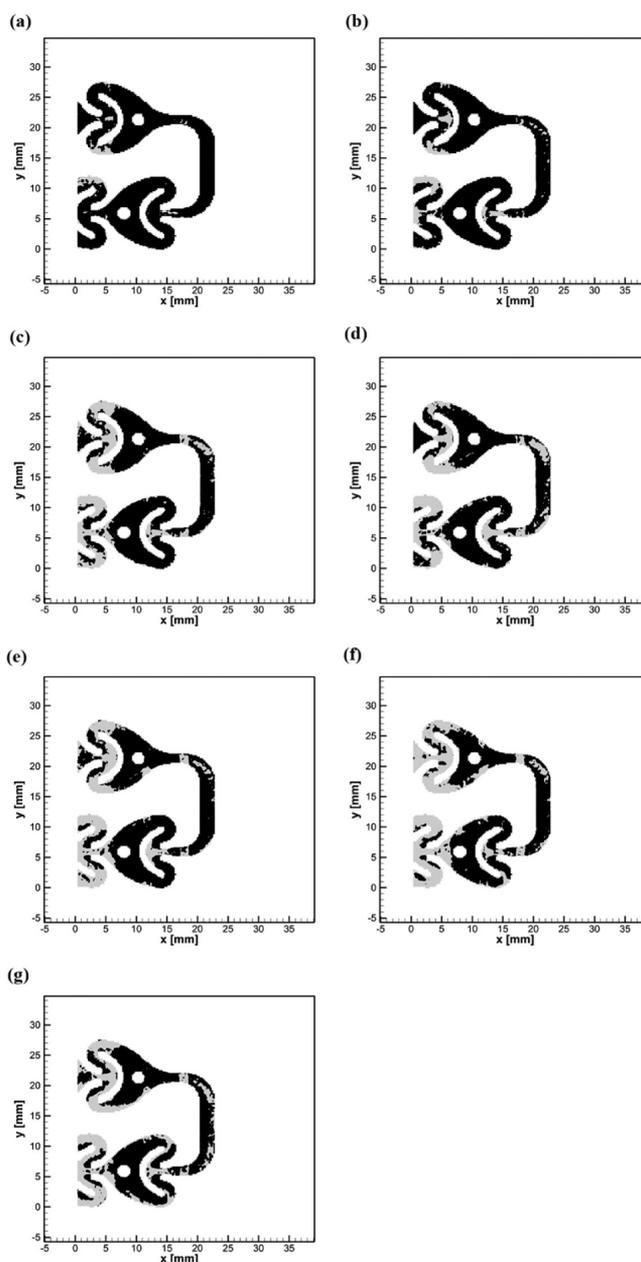
Table 3. Bubble Statistics for a Gas Volume Transport Fraction of β = 0.25 and Flow Rates from 10 to 40 mL/min

flow rate (mL/min)	no. of bubbles	number-averaged bubble size (mm)	standard deviation (mm)
10	14	2.379	1.009
15	15	2.296	0.614
20	17	2.288	0.741
25	22	1.801	0.596
30	26	1.636	0.836
35	30	1.342	0.503
40	36	1.297	0.416
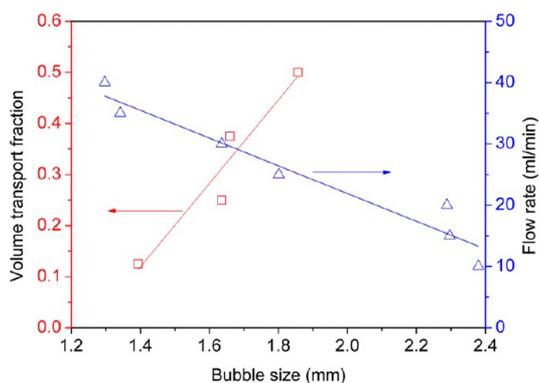
Figure 14. Relationship of bubble size to gas volume transport fraction at a fixed flow rate of 30 mL/min (red) and flow rate at a fixed gas volume transport fraction of 0.25 (blue).

Figure 15. Ratios of the RMS velocity fluctuation magnitudes (two-phase flow/single-phase flow) for a gas volume transport fraction of β = 0.25 at different overall flow rates: (a) 10 mL/min; (b) 15 mL/min; (c) 20 mL/min; (d) 25 mL/min; (e) 30 mL/min; (f) 35 mL/min; (g) 40 mL/min. Dark regions indicate ratios larger than 1, and light regions indicate ratios smaller than 1.

single-phase flow are depicted in Figure 15. As introduced in Figure 12, dark regions represent values of the ratio greater than 1, i.e., increased mixing in the case of two-phase flow, whereas light regions indicate reduced mixing in the case of two-phase flow. The overall trend is similar to that observed for constant flow rate and changing gas volume transport fraction (Figure 12). Quite notably, it was found that for overall flow rates of 10 and 15 mL/min, the ratio in almost the entire region of interest exceeds 1, which means that at low flow rates the introduction of the gas phase also increases the velocity fluctuations in the inlet and outlet sections of the heart cell. This is explained by the fact that at low flow rates the largest

bubble sizes are obtained (see Table 3), and consequently, the effect of the dispersion on the continuous phase is pronounced.

The average RMS velocity fluctuation magnitudes and their standard deviations are listed in Table 4. For flow rates larger than 15 mL/min, introducing a gas phase does not increase the average RMS velocity fluctuation magnitude but does reduce the standard deviation. However, for flow rates of 10 and 15 mL/min, there is an increase in the average RMS velocity as well as a decrease in the standard deviation. This also highlights the fact that the impact of introducing a gas phase is more pronounced at low flow rates, most likely as a result of the increased bubble size (Table 3). In addition, it was observed that the average RMS velocity is a function of the overall flow

Table 4. Average RMS Velocity Fluctuation Magnitudes and Standard Deviations in the ROI for Single-Phase Flow and Two-Phase Flow at a Gas Volume Transport Fraction of $\beta = 0.25$

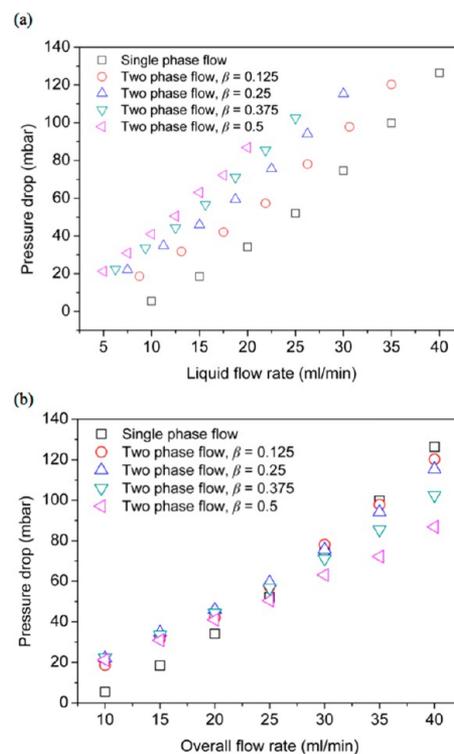|	single-phase flow		two-phase flow ($\beta = 0.25$)	
flow rate (mL/min)	average RMS velocity fluctuation magnitude (m/s)	standard deviation (m/s)	average RMS velocity fluctuation magnitude (m/s)	standard deviation (m/s)
10	0.0209	0.0305	0.0306	0.0100
15	0.0257	0.0348	0.0360	0.0109
20	0.0464	0.0565	0.0397	0.0118
25	0.0553	0.0711	0.0418	0.0187
30	0.0693	0.0871	0.0522	0.0154
35	0.0993	0.1173	0.0599	0.0178
40	0.0970	0.1069	0.0745	0.0241
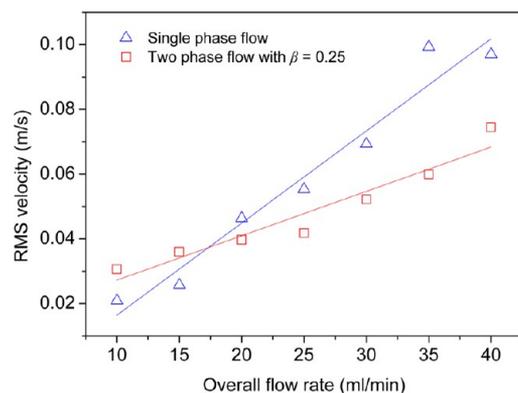
Figure 16. Relationship between the RMS velocities for single- and two-phase flow and the overall flow rate.

rate, as it increases linearly with increasing flow rate for both single- and two-phase flow (see Figure 16).

Experimental Pressure Drops for Single- and Two-Phase Flow in the AFR. Figure 17 depicts the experimentally determined pressure drops for single- and two-phase flow in the AFR. When the pressure drop is plotted versus the liquid-phase flow rate (Figure 17a), the additional contribution to the pressure drop due to the presence of the dispersed gas phase is observed. In general, the total pressure drop can be attributed to two major interactions: first, the frictional interaction of the continuous liquid phase with the walls in the AFR structure, and second, the interaction of the continuous liquid phase with the dispersed gas phase. The latter is nonexistent for single-phase flow, as can be observed in Figure 17a.

Figure 17b depicts the experimentally determined pressure drops subject to the overall flow rate (gas and liquid phase). When the gas volume transport fraction is kept constant, the pressure drop increases with the overall flow rate because of the increase in the frictional interaction of the liquid phase with the wall and the increased interaction between the two phases.

Investigation of the relative influence of the phase interaction on the total pressure drop showed that at a constant overall flow rate, increasing the gas volume transport fraction has no significant effect, and thus, a larger liquid flow rate results in a larger pressure drop. For the AFR, this effect is more pronounced when the overall flow rate is larger than 30 mL/min. When two-phase flow and single-phase flow at the same overall flow rate are compared, a critical flow rate of around 25 mL/min is observed. Below this critical flow rate, the pressure

Figure 17. Experimental pressure drop results for single- and two-phase flow in the AFR: (a) pressure drop vs liquid phase flow rate; (b) pressure drop vs overall flow rate (gas and liquid phase).

drop for single-phase flow is lower than that for two-phase flow, as the contribution to the pressure drop due to the phase interaction is more dominant at low flow rates (see Figure 17b).

■ CONCLUSION

In this work, the flow field in the Corning AFR was for the first time characterized using PIV for both single- and two-phase flow. The single-phase experimental results match well with established CFD simulation methods, validating the PIV results for such a challenging optical arrangement. At the flow rates investigated, the velocity field is almost symmetric in the heart-shaped cells for single-phase flow, and the presence of the U-shaped structure and the post creates a stagnation zone in between them that is detrimental for mixing purposes. The addition of the gas phase greatly increases the momentum exchange in the heart cells, which is quantified in terms of the RMS velocity fluctuation magnitude. For overall flow rates below 15 mL/min, the two-phase flow hydrodynamics exhibits larger momentum exchange in the entire AFR structure, which is linked to the impact of the increased bubble size in this flow rate range on the continuous bulk phase. When the overall flow rate exceeds 15 mL/min, the overall RMS velocity fluctuation magnitude in single-phase flow is larger than that in two-phase flow, but its standard deviation is reduced in the case of two-phase flow, which leads to a more uniform distribution of velocity fluctuations and associated transport processes within the AFR.

The results obtained in this work provide a detailed understanding of the two-phase flow hydrodynamics and transport processes in the AFR. Furthermore, the PIV results can be used for the validation of gas−liquid two-phase flow

CFD simulations that can constitute the basis of future improvements in the Corning AFR design.

■ AUTHOR INFORMATION

Corresponding Author
*E-mail: simon.kuhn@cit.kuleuven.be.

Notes
The authors declare no competing financial interest.

■ NOTATION

Abbreviations
AFR = Advanced-Flow reactor
CCD = charge-coupled device
CFD = computational fluid dynamics
PIV = particle image velocimetry
RMS = root-mean-square
ROI = region of interest

Roman Symbols
d = bubble size, mm
D = hydrodynamic diameter of the nozzle, mm
h = channel height, mm
k_La = interfacial mass transfer coefficient, s^{-1}
l = hydrodynamic diameter of liquid inlet, mm
u = inlet liquid velocity, m/s
$\overline{u}$ = mean experimental velocity in the x direction, m/s
u_{rms} = RMS velocity fluctuation, m/s
U = velocity, m/s
$\overline{U}$ = mean part of the velocity, m/s
U' = fluctuating part of the velocity, m/s
U_{rms} = magnitude of the RMS velocity fluctuation vector, m/s
$\overline{v}$ = mean experimental velocity in the y direction, m/s
$\dot{V}_G$ = gas flow rate, mL/min
$\dot{V}_L$ = liquid flow rate, mL/min
w = channel width, mm
x = x direction of the AFR, mm
y = y direction of the AFR, mm
z = z direction of the AFR, mm

Greek Letters
β = gas volume transport fraction
λ = wavelength, nm

■ REFERENCES

(1) Elvira, K. S.; Casadevall i Solvas, X.; Wootton, R. C. R.; deMello, A. J. The past, present and potential for microfluidic reactor technology in chemical synthesis. *Nat. Chem.* **2013**, *5*, 905.

(2) Jensen, K. F. Microreaction engineering - is small better? *Chem. Eng. Sci.* **2001**, *56*, 293.

(3) Wu, K. J.; Kuhn, S. Strategies for solids handling in microreactors. *Chim. Oggi* **2014**, *32* (3), 62.

(4) Hessel, V.; Löb, P.; Löwe, H., Industrial Microreactor Process Development Up to Production. In *Micro Process Engineering*; Wiley-VCH: Weinheim, Germany, 2009; p 181.

(5) Chen, Q.-L.; Wu, K.-J.; He, C.-H. Investigation on liquid flow characteristics in microtubes. *AIChE J.* **2015**, *61*, 718.

(6) Monbaliu, J. C. M. R.; Winter, M.; Chevalier, B.; Schmidt, F.; Jiang, Y.; Hoogendoorn, R.; Kousemaker, M.; Stevens, C. V. Feasibility study for industrial production of fuel additives from glycerol. *Chim. Oggi* **2010**, *28* (4), 8.

(7) Wirth, T. *Microreactors in Organic Chemistry and Catalysis*; Wiley-VCH: Weinheim, Germany, 2013.

(8) Prat, L.; Devatine, A.; Cognet, P.; Cabassud, M.; Gourdon, C.; Elgue, S.; Chopard, E. Performance evaluation of a novel concept "open plate reactor" applied to highly exothermic reactions. *Chem. Eng. Technol.* **2005**, *28*, 1028.

(9) Thayer, A. M. HARNESSING MICROREACTIONS. *Chem. Eng. News.* **2005**, *83* (22), 43.

(10) Stange, O.; Schael, F.; Herbstritt, F.; Gasche, H.; Boonstra, E.; Mukherjee, S. Modular Micro Process Technology—New Devices and Applications. Presented at IMRET-10: 10th International Conference on Microreaction Technology, New Orleans, LA, 2008.

(11) Hessel, V.; Angeli, P.; Gavriilidis, A.; Löwe, H. Gas–Liquid and Gas–Liquid–Solid Microstructured Reactors: Contacting Principles and Applications. *Ind. Eng. Chem. Res.* **2005**, *44*, 9750.

(12) Odille, F. G. J.; Stenemyr, A.; Pontén, F. Development of a Grignard-Type Reaction for Manufacturing in a Continuous-Flow Reactor. *Org. Process Res. Dev.* **2014**, *18*, 1545.

(13) Rossi, E.; Woehl, P.; Maggini, M. Scalable in Situ Diazomethane Generation in Continuous-Flow Reactors. *Org. Process Res. Dev.* **2012**, *16*, 1146.

(14) Santiago, J. G.; Wereley, S. T.; Meinhart, C. D.; Beebe, D. J.; Adrian, R. J. A particle image velocimetry system for microfluidics. *Exp. Fluids* **1998**, *25*, 316.

(15) van Steijn, V.; Kreutzer, M. T.; Kleijn, C. R. mu-PIV study of the formation of segmented flow in microfluidic T-junctions. *Chem. Eng. Sci.* **2007**, *62*, 7505.

(16) Meinhart, C. D.; Wereley, S. T.; Santiago, J. G. PIV measurements of a microchannel flow. *Exp. Fluids* **1999**, *27*, 414.

(17) Kuhn, S.; Jensen, K. F. A pH-Sensitive Laser-Induced Fluorescence Technique To Monitor Mass Transfer in Multiphase Flows in Microfluidic Devices. *Ind. Eng. Chem. Res.* **2012**, *51*, 8999.

(18) Sebastian Cabeza, V.; Kuhn, S.; Kulkarni, A. A.; Jensen, K. F. Size-Controlled Flow Synthesis of Gold Nanoparticles Using a Segmented Flow Microfluidic Platform. *Langmuir* **2012**, *28*, 7007.

(19) Zhang, F.; Cerato-Noyerie, C.; Woehl, P.; Lavric, E. D. Intensified Liquid/Liquid Mass Transfer in Corning Advanced-Flow Reactors. *Chem. Eng. Trans.* **2011**, *24*, 1369.

(20) Chivilikhin, M. S.; Soboleva, V.; Kuandykov, L.; Woehl, P.; Lavric, E. D. CFD analysis of hydrodynamic and thermal behaviour of Advanced-Flow Reactors. *Chem. Eng. Trans.* **2010**, *21*, 1099.

(21) Nieves-Remacha, M. J.; Kulkarni, A. A.; Jensen, K. F. Gas-Liquid Flow and Mass Transfer in an Advanced-Flow Reactor. *Ind. Eng. Chem. Res.* **2013**, *52*, 8996.

(22) Nieves-Remacha, M. J.; Kulkarni, A. A.; Jensen, K. F. Hydrodynamics of Liquid-Liquid Dispersion in an Advanced-Flow Reactor. *Ind. Eng. Chem. Res.* **2012**, *51*, 16251.

(23) Woitalka, A.; Kuhn, S.; Jensen, K. F. Scalability of mass transfer in liquid-liquid flow. *Chem. Eng. Sci.* **2014**, *116*, 1.

(24) Günther, A.; Jhunjhunwala, M.; Thalmann, M.; Schmidt, M. A.; Jensen, K. F. Micromixing of miscible liquids in segmented gas-liquid flow. *Langmuir* **2005**, *21*, 1547.

(25) Assmann, N.; von Rohr, P. R. Extraction in microreactors: Intensification by adding an inert gas phase. *Chem. Eng. Process.* **2011**, *50*, 822.

(26) Su, Y. H.; Chen, G. W.; Yuan, Q. Influence of hydrodynamics on liquid mixing during Taylor flow in a microchannel. *AIChE J.* **2012**, *58*, 1660.

(27) Deen, N. G.; Willems, P.; Annaland, M. v. S.; Kuipers, J. A. M.; Lammertink, R. G. H.; Kemperman, A. J. B.; Wessling, M.; van der Meer, W. G. J. On image pre-processing for PIV of single- and two-phase flows over reflecting objects. *Exp. Fluids* **2010**, *49*, 525.

(28) Nogueira, S.; Sousa, R. G.; Pinto, A. M. F. R.; Riethmuller, M. L.; Campos, J. B. L. M. Simultaneous PIV and pulsed shadow technique in slug flow: a solution for optical problems. *Exp. Fluids* **2003**, *35*, 598.

(29) Abramoff, M. D.; Magalhaes, P. J.; Ram, S. J. Image processing with ImageJ. *Biophotonics Int.* **2004**, *11*, 36.

(30) http://www.openfoam.org.

(31) Su, Y. H.; Chen, G. W.; Kenig, E. Y. An experimental study on the numbering-up of microchannels for liquid mixing. *Lab Chip* **2015**, *15*, 179.

(32) van Steijn, V.; Kleijn, C. R.; Kreutzer, M. T. Predictive model for the size of bubbles and droplets created in microfluidic T-junctions. *Lab Chip* **2010**, *10*, 2513.

(33) Wols, B. *Computational Fluid Dynamics in Drinking Water Treatment*; IWA Publishing: London, 2011.